J. Fluid Mech. (2005), *vol.* 543, *pp.* 93–106. © 2005 Cambridge University Press
doi:10.1017/S0022112005006440 Printed in the United Kingdom

Reynolds number effect on drag reduction in a microbubble-laden spatially developing turbulent boundary layer

By ANTONINO FERRANTE AND SAID ELGHOBASHI

Department of Mechanical and Aerospace Engineering,
University of California, Irvine, CA 92697, USA

(Received 21 March 2005 and in revised form 28 June 2005)

We have performed direct numerical simulations for a microbubble-laden spatially developing turbulent boundary layer (SDTBL) and compared the amount of skin friction reduction due to the presence of the bubbles for two Reynolds numbers: $Re_\theta = 1430$ and $Re_\theta = 2900$. The results show that increasing the Reynolds number decreases the percentage of drag reduction. Increasing Re_θ 'squeezes' the quasi-streamwise vortical structures toward the wall, whereas the microbubbles 'push them away' from the wall. The net result of these two opposing effects determines the amount of skin friction reduction by the microbubbles. The displacement of the vortical structures by the microbubbles is a result of the local positive velocity divergence, $\nabla \cdot \boldsymbol{U}$, created by the bubble concentration gradients. Thus, the volume fraction of bubbles that is responsible for the reduction of skin friction in a SDTBL at a given Reynolds number is not sufficient to produce the same amount of reduction in skin friction at higher Reynolds number.

1. Introduction

In a recent paper (Ferrante & Elghobashi 2004*b*, hereinafter referred to as FE), we reported the results of a direct numerical simulation (DNS) study to explain the physical mechanisms responsible for the reduction of skin friction in a microbubble-laden, spatially developing turbulent boundary layer (SDTBL) of a liquid flow over a flat plate at $Re_\theta = 1430$ (or $Re_x \approx 8 \times 10^5$). The objective of the present paper is to examine the effect of increasing Re_θ on the reduction of skin friction in the microbubble-laden SDTBL. We increase Re_θ to more than double its value in FE, i.e. to $Re_\theta = 2900$ (or $Re_x \approx 2 \times 10^6$).

The motivation for the present study is to answer the following questions:

(i) If both the bubble diameter and bubbles volume fraction are kept constant, would the reduction in skin friction decrease or increase on increasing the Reynolds number of a SDTBL over a flat plate?

(ii) What are the physical mechanisms causing the increase or decrease?

At present there are no published experimental, numerical or analytical studies that can answer these questions.

The experimental study of Madavan, Deutsch & Merkle (1985) (the only published detailed results on the subject) shows that, for a given volume fraction of injected air, increasing the liquid free-stream velocity, U_∞, from 10.8 to 16.7 m s^{-1} decreases the amount of skin friction reduction (see their Figures 8 and 9, p. 245). However, these

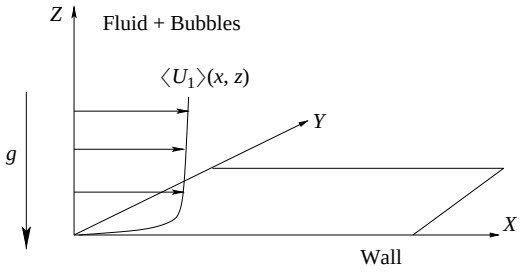

FIGURE 1. Schematic of bubble-laden turbulent boundary layer flow over a flat wall.

results could not answer the above questions since the diameter of a bubble created by injecting air into an orifice or a porous plate, as was the case in the experiment, decreases as the shear stress at the plate increases due to the higher U_∞ (Hinze 1955; Silberman 1957; Pal, Merkle & Deutsch 1988; Martinez-Bazan, Montanes & Lasheras 1999). In other words, the experimental results of Madavan *et al.* (1985) do not distinguish between the simultaneous and most probably opposing effects of increasing the Reynolds number of the SDTBL and decreasing the bubble diameter on the reduction of the skin friction at the plate. It should be noted that our earlier DNS study (Ferrante & Elghobashi 2004*a*) of the effects of bubble diameter on the reduction of skin friction in the SDTBL indicates that the smaller the bubble diameter, the larger the reduction in skin friction.

Our new DNS results, to be presented in the following sections, show that increasing the Reynolds number from $Re_\theta = 1430$ (or $Re_x \approx 8 \times 10^5$) to $Re_\theta = 2900$ (or $Re_x \approx 2 \times 10^6$), while fixing the bubbles diameter and volume fraction, decreases the amount of drag reduction in the microbubble-laden SDTBL over a flat plate. We explain in § 3 the physical mechanisms responsible for this Reynolds number effect.

2. Mathematical description

Figure 1 shows a schematic of the SDTBL flow where the gravitational acceleration vector is perpendicular to the wall, and pointing downwards.

We employ the Eulerian–Lagrangian approach in which we solve the fluid continuity and momentum equations, (2.1) and (2.2), in an Eulerian framework, whereas the bubble acceleration equation, (2.3), is solved for each bubble to track its trajectory in time. The equations governing the motion of a spatially developing bubble-laden turbulent boundary layer can be written in non-dimensional form as (Ferrante 2004):

carrier fluid continuity,

$$\partial_t(1-C) + \partial_j[(1-C)\,U_j] = 0, \tag{2.1}$$

carrier fluid momentum,

$$\partial_t[(1-C)U_i] + \partial_j[(1-C)U_iU_j] = -(1-C)\;\partial_i P + \nu\,\partial_j[(1-C)(\partial_j U_i + \partial_i U_j)] - f_i + (1-C)g_i, \tag{2.2}$$

bubble acceleration,

$$\frac{\mathrm{d}V_i}{\mathrm{d}t} = 3\frac{\mathrm{D}U_{s,i}}{\mathrm{D}t} + \frac{1}{\tau_b}(U_{s,i} - V_i + V_t) + [(\boldsymbol{U_s} - \boldsymbol{V}) \times \boldsymbol{\Omega_s}]_i. \tag{2.3}$$

In the above equations, U_i are the components of instantaneous fluid (liquid) velocity and P is the pressure. $C(x, y, z, t)$ is the instantaneous local bubble-phase

Re_δ	$\nu = 1/Re_\delta$	$u_{\tau 0}$	$\check{\delta}_0$(mm)	$\check{U}_\infty$(m s^{-1})	$\check{d}_b$(μm)	d_b^+	τ_b^+
8×10^3	1.25×10^{-4}	0.0464	9.7	0.83	40	1.54	0.065
19×10^3	5.26×10^{-5}	0.0425	9.7	1.97	40	3.34	0.307

TABLE 1. Fluid and bubble properties.

Re_δ	L_x	L_y	L_z	N_x	N_y	N_z	Δx^+	Δy^+	z^+_{min}
8×10^3	$20\,\delta_0$	$5\,\delta_0$	$7\,\delta_0$	1024	512	128	7.25	3.6	0.58
19×10^3	$20\,\delta_0$	$5\,\delta_0$	$7\,\delta_0$	1024	512	128	15.8	7.9	1.26

TABLE 2. Computational mesh details.

concentration (or volume fraction) computed from the local number of bubbles N_b in a given computational cell of volume $\mathscr{V}_c$ as $C(\boldsymbol{x}, t) = N_b(\boldsymbol{x}, t)\,[\pi d_b^3/6]\,/\,\mathscr{V}_c(\boldsymbol{x})$, where d_b is the bubble diameter. The dimensionless kinematic viscosity is $\nu = 1/Re_\delta$ where $Re_\delta = \check{U}_\infty \check{\delta}_0/\check{\nu}$ is the Reynolds number based on the dimensional free-stream velocity $\check{U}_\infty$, boundary layer thickness (based on the location of 99% of the free-stream velocity) $\check{\delta}_0$ at the inlet plane ($x = 0$) of the computational domain, and kinematic viscosity $\check{\nu}$ ($= 10^{-6}\,\mathrm{m^2\,s^{-1}}$). All variables in (2.1)–(2.3) and throughout the paper are non-dimensionalized by $\check{U}_\infty$ and $\check{\delta}_0$ (table 1). The force f_i in (2.2) is imparted by the bubbles to the surrounding fluid, and is calculated according to Druzhinin & Elghobashi (1998) as $-f_i = C(\mathrm{D}U_{s,i}/\mathrm{D}t - g_i)$, where g_i is the component of the gravitational acceleration in the i-direction, $g_i = -g\delta_{iz}$ (figure 1), where g is the dimensionless gravitational acceleration. In (2.3) $\boldsymbol{U_s}$ and $\boldsymbol{\Omega_s}$ are respectively the instantaneous fluid velocity and fluid vorticity at the bubble location, $\boldsymbol{x}_b(t)$, and $\boldsymbol{V}$ is the bubble instantaneous velocity. Also, $\mathrm{d}/\mathrm{d}t \equiv \partial_t + V_j\,\partial_j$ is the time derivative in a frame moving with the bubble, $\mathrm{D}/\mathrm{D}t \equiv \partial_t + U_j\,\partial_j$ is the time derivative following a fluid element. The bubble response time τ_b is defined according to Stokes drag law as $\tau_b = d_b^2\,/\,(36\,\nu)$ (table 1). The terminal velocity $V_t = -2\tau_b\,g_i$. Throughout the paper, dimensionless quantities in wall units carry the superscript +, i.e. $U_1^+ = U_1/u_\tau$, $z^+ = zu_\tau/\nu$ and $t^+ = tu_\tau^2/\nu$, where u_τ is the wall friction velocity.

The computational domain is a parallelepiped whose dimensions L_x, L_y and L_z, and the corresponding numbers of grid points, N_x, N_y and N_z in the streamwise, spanwise and wall-normal directions respectively are listed in table 2. The computational mesh is equispaced in the streamwise and spanwise directions, with grid spacings Δx^+ and Δy^+ (table 2), whereas in the vertical direction, the mesh is stretched gradually via mapping a uniform computational grid ζ onto its non-uniform counterpart z with a combination of hyperbolic tangent functions (Ferrante & Elghobashi 2004*c*) up to $z = 3.6\,\delta_0$ using 96 mesh points, above which a quadratic grid function is applied.

The initial ($t = 0$) velocity field of the fluid throughout the domain was identical to the instantaneous velocity field ($t = 160$) computed by DNS of the single-phase SDTBL ($\phi_v = 0$) at the same Re_δ on the same mesh (table 2). The boundary conditions and the generation of the turbulent flow conditions at the inlet plane ($x = 0$) are described in detail by Ferrante & Elghobashi (2004*c*).

At time $t = 0$ the bubbles were released randomly in the computational domain inside the boundary layer zone ($z < \delta_0 = 1$), with each bubble velocity component set equal to that of the fluid at the bubble location. In order to keep the average volume

Case	Re_δ	$Re_\theta(x = 0)$	ϕ_v	N_B	$(C_{f,SPF} - C_f)/C_{f,SPF}$
A	8×10^3	1020	0	0	0
B	8×10^3	1020	0.01	29×10^6	22%
C	19×10^3	2340	0	0	0
D	19×10^3	2340	0.01	29×10^6	19%

TABLE 3. Physical parameters for the four cases (A–D) studied and reductions of skin friction.

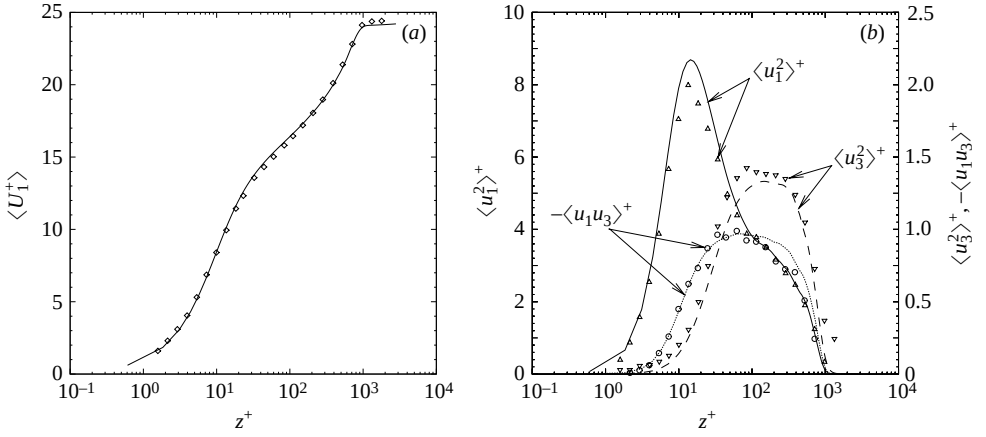

FIGURE 2. (*a*) Mean streamwise velocity profile at $Re_\theta = 2900$; (*b*) Reynolds stresses profiles at $Re_\theta = 2900$. Present DNS, case C (lines); experimental data of DeGraaff & Eaton (2000) (symbols).

fraction of bubbles in the computational domain, ϕ_v, constant in time, when a bubble exits one of the domain boundaries it is reinjected at a random location inside the boundary layer according to a semi-Gaussian distribution for the streamwise location, except for the spanwise boundaries ($y = 0$ and $y = L_y$) where periodicity was applied. The details of our numerical method are provided in the Appendix.

3. Results

The parameters (Re_δ, ϕ_v, N_B), Re_θ at the inflow plane $x = 0$, and the percentage reduction of skin friction in the four test cases studied are listed in table 3. N_B is the total number of bubbles in the computational domain. table 1 shows the properties of the bubbles used in the present study. In tables 1 and 2 the variables written in wall units were non-dimensionalized using the dimensionless friction velocity at the inflow plane, u_{τ_0}, and ν (table 1).

3.1. *Single-phase SDTBL: comparison with experiments*

We first validate our DNS results for the single-phase SDTBL before presenting the results for the bubble-laden flow. We compare our DNS results for the single-phase SDTBL (case C) with the experimental data of DeGraaff & Eaton (2000) for $Re_\theta = 2900$. For this case C we used $N_z = 192$ and $L_z = 3.6$ ($z^+_{min} = 0.6$). We write the fluid velocity component, U_i, as the sum of its mean and fluctuation, $U_i(x, y, z, t) = \langle U_i \rangle(x, z) + u_i(x, y, z, t)$, where $\langle \ldots \rangle$ represents, throughout the paper, spatial averaging in the spanwise (y) direction in addition to time averaging of the enclosed quantity, and u_i is the local instantaneous deviation from $\langle U_i \rangle$. Figure 2

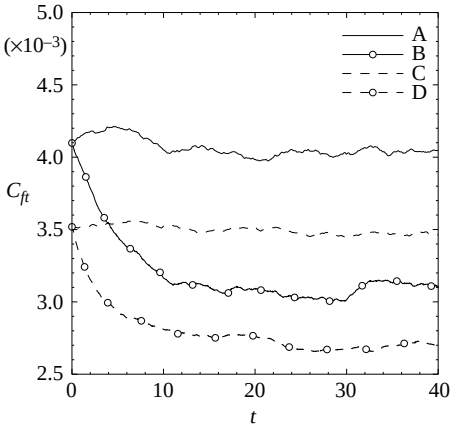

FIGURE 3. Temporal distribution of skin friction, C_{ft}, for single-phase and bubble-laden SDTBL, for $Re_\theta = 1430$ and $Re_\theta = 2900$.

displays the comparison in wall units for the mean streamwise velocity, $\langle U_1 \rangle^+$, and three Reynolds stresses at $x = 14$, where $Re_\theta = 2900$. The mean velocity profile is in excellent agreement with the experimental profile. The agreement for the Reynolds stresses $\langle u_1^2 \rangle^+$, $\langle u_3^2 \rangle^+$ and $\langle u_1 u_3 \rangle^+$ is very good especially for the locations of the peaks of the three profiles. Our computed skin friction coefficient ($C_{fx} = 2\,\tau_w/(\rho\, U_\infty^2) = 3.41 \times 10^{-3}$, where $\tau_w = \mu[\partial_z \langle U_1 \rangle(x, z)]_{z=0}$) at $Re_\theta = 2900$ is in excellent agreement with that measured ($C_{fx} = 3.36 \times 10^{-3}$) by DeGraaff & Eaton (2000). It should be mentioned that our present DNS results are the first to be reported for such relatively high $Re_\theta = 2900$ (or $Re_x \approx 2 \times 10^6$).

3.2. *Microbubble-laden SDTBL*

The temporal development of the skin friction coefficient, C_{ft}, defined as

$$C_{ft} = \frac{2}{(\rho\, U_\infty^2)} \frac{1}{L_x L_y} \int_0^{L_x} \int_0^{L_y} \tau_w(x, y, t)\, \mathrm{d}y\, \mathrm{d}x, \tag{3.1}$$

where $\tau_w(x, y, t) = \mu[\partial_z U_1(x, y, t)]_{z=0}$, is shown in figure 3 for both $Re_\theta = 1430$ and $Re_\theta = 2900$. The figure shows that doubling Re_θ reduces the percentage of skin friction reduction, e.g. from 27 % to 23 % at $t = 30$. Defining

$$C_f = \frac{1}{T} \int_0^T C_{ft}\, \mathrm{d}t$$

as a time-average of C_{ft} we find that doubling Re_θ reduces the percentage of skin friction reduction from 22 % to 19 % (table 3). Since the DNS of both flows used the same bubble volume fraction and the same bubble diameter then the above result is due only to increasing Re_θ. Our objective now is to explain how the increase of Re_θ decreases the amount of skin-friction reduction. It should be noted that the percentage reduction in skin friction for $Re_\theta = 1430$ here (case B) is larger than that (12%) for case C in our earlier study (FE). The reason is that the bubble diameter used here equals nearly two thirds of its value in FE (Ferrante & Elghobashi 2004*a*). Our earlier DNS results (FE) for the microbubble-laden SDTBL for $Re_\theta = 1430$ with volume fraction ranging from $\phi_v = 0.001$ to 0.02 show that the presence of bubbles results in a local positive divergence of the fluid velocity, $\nabla \cdot \boldsymbol{U} > 0$, creating a positive mean velocity, $\langle U_3 \rangle$, normal to (and away from) the wall which, in turn, reduces

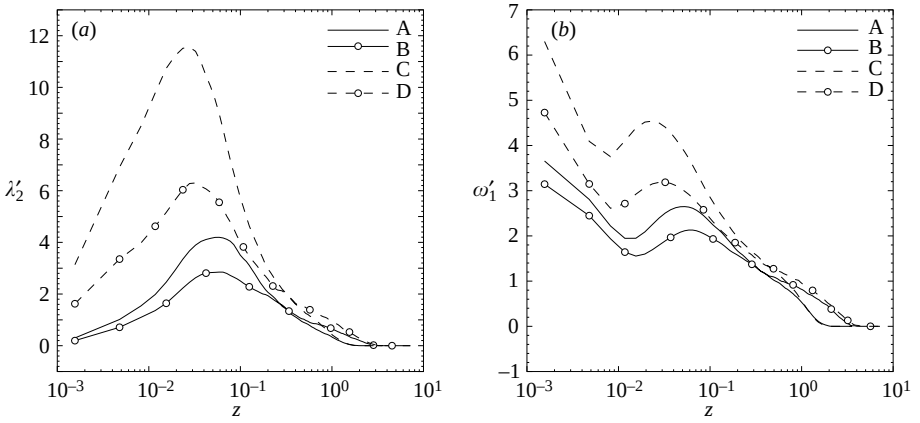

FIGURE 4. Profiles of $\lambda_2'(z)$ and $\omega_1'(z)$ at $x = 18.9$ for $Re_\theta = 1430$ and $Re_\theta = 2900$.

the mean streamwise velocity and displaces the quasi-streamwise longitudinal vortical structures away from the wall. We identified the quasi-streamwise vortical structures using the method of Jeong & Hussain (1995), who defined λ_2 as the second largest eigenvalue of the tensor $(S_{ik}S_{kj} + \Omega_{ik}\Omega_{kj})$, where $S_{ij} \equiv (\partial_j U_i + \partial_i U_j)/2$ is the strain rate tensor, and $\Omega_{ij} \equiv (\partial_j U_i - \partial_i U_j)/2$ is the rotation rate tensor. Jeong & Hussain (1995) showed that connected flow regions of negative values of λ_2 identify the cores of the vortical structures. We applied this method to our SDTBL flow, and observed that the vortical structures populating the buffer layer in the bubble-laden SDTBL remain almost aligned with the streamwise direction (quasi-streamwise vortical structures) as in the single-phase SDTBL. This was indicated by the profiles of the correlation coefficients, R_i (Jeong, Hussain & Kim 1997), between $-\lambda_2$ and the absolute values of the vorticity components, ω_i, as they remain nearly identical for the single-phase and bubble-laden SDTBLs.

The displacement of the quasi-streamwise vortical structures away from the wall has the following two main effects:

(i) it increases the spanwise gaps between the wall streaks associated with the sweep events and reduces the streamwise velocity in these streaks, thus reducing the skin friction by up to 12 % for $\phi_v = 0.01$ and about 20 % for $\phi_v = 0.02$;

(ii) it moves the location of the peak Reynolds stress production rate away from the wall to a zone of a smaller transverse gradient of the mean streamwise velocity (i.e. smaller mean shear), thus reducing the production rate of turbulence kinetic energy and enstrophy.

Now since the displacement of vortical structures away from the wall is the key mechanism for drag reduction we need to examine the effect of increasing Re_θ on the eigenvalue λ_2. Figure 4(*a*) shows the profiles of $\lambda_2'(z)$, the root mean square of λ_2, for both the single-phase and bubble-laden SDTBLs for the two cases of $Re_\theta = 1430$ and $Re_\theta = 2900$. We see that doubling Re_θ in the single-phase SDTBL nearly triples the maximum value of $\lambda_2'(z)$ and displaces the profile peak toward the wall from $z = 0.06$ to $z = 0.025$. Both the magnitude and location of the $\lambda_2'(z)$ peak are dictated by the magnitudes and locations of the maximum values of ω_1' (figure 4*b*) and $(\partial U_1/\partial z)$ (figure 5*b*) according to the above definition of $\lambda_2'(z)$. Note that all the profiles of $\omega_1'(z)$ (figure 4*b*) display two peaks: one, in the buffer layer, aligned with the peak of $\lambda_2'(z)$, created by the quasi-streamwise vortical structures, and another at the wall,

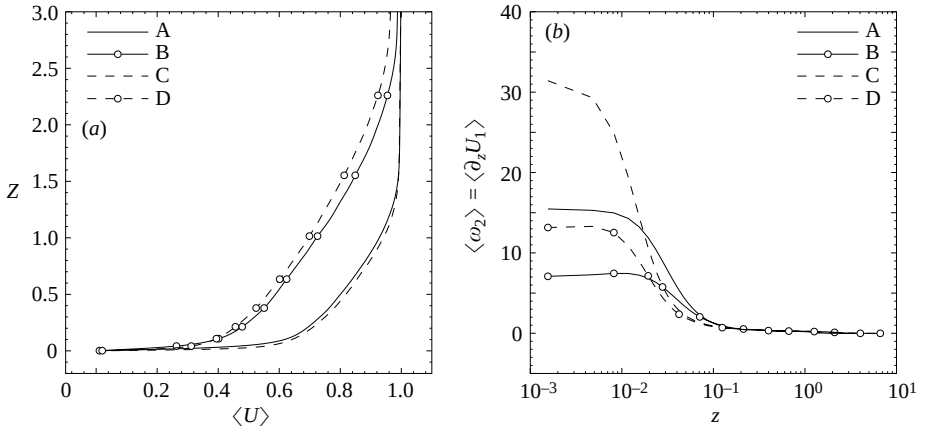

FIGURE 5. Profiles of mean velocity $\langle U_1 \rangle(z)$ and mean velocity gradient $\langle \partial U_1/\partial z \rangle$ at $x = 18.9$ for $Re_\theta = 1430$ and $Re_\theta = 2900$.

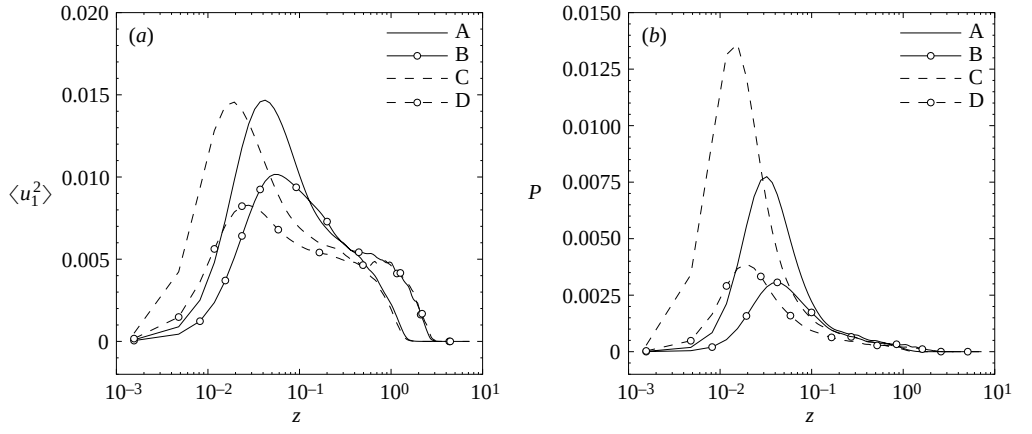

FIGURE 6. Profiles of Reynolds stress $\langle u_1^2 \rangle(z)$ and production rate of turbulence kinetic energy at $x = 18.9$ for $Re_\theta = 1430$ and $Re_\theta = 2900$.

with larger magnitude resulting from the opposite-signed ω_1' generated by the no-slip condition. The displacement of the $\lambda_2'(z)$ profile peak toward the wall with the increase of Re_θ in the single-phase SDTBL is due to the fact that the zone containing the steepest gradient $(\partial U_1/\partial z)$ moves closer to the wall (figure 5*b*) (see the above definition of λ_2) as the Reynolds number increases since the enhanced turbulent mixing brings higher velocity fluid closer to the wall (figure 5*a*). This displacement is clearly manifested in the similar displacements of the profiles of the Reynolds stresses $\langle u_1^2 \rangle(z)$ (figure 6*a*) and production rate, $P(z)$, of turbulence kinetic energy (figure 6*b*). It should be noted that if the profiles in Figures 4 and 6 were plotted vs. z^+ instead of z these displacements would have been masked since the viscous length scale $(\ell = \nu/u_\tau)$ decreases with increasing Re_θ, and $z^+ = z/\ell$.

It is now clear that in the single-phase SDTBL, the higher the Reynolds number, the closer to the wall the quasi-streamwise longitudinal vortical structures are. This finding is confirmed by plotting the contours (not shown here) of the instantaneous vorticity ω_1 in a vertical, (y, z), plane for both $Re_\theta = 1430$ and 2900.

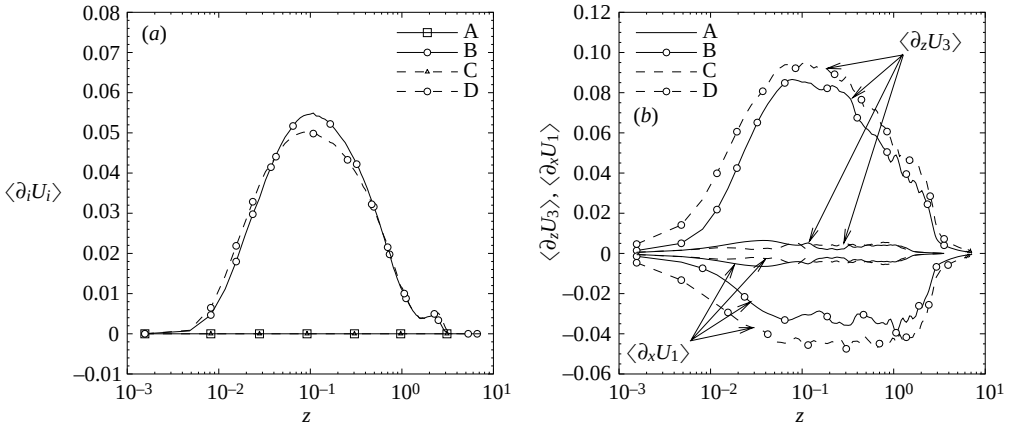

FIGURE 7. Profiles of $(\nabla \cdot \boldsymbol{U})$, $(\partial W/\partial z)$ and $(\partial U/\partial x)$ at $x = 18.9$ for $Re_\theta = 1430$ and $Re_\theta = 2900$.

In the bubble-laden SDTBL, as mentioned above and discussed in FE, microbubbles reduce the skin friction by displacing the vortical structures away from the wall. Again, this is confirmed by plotting the contours (not shown) of the instantaneous vorticity ω_1 in a vertical, (y, z), plane for both $Re_\theta = 1430$ and 2900. The contours indicate that most of the structures with the largest ω_1 magnitude in the high-Reynolds-number, $Re_\theta = 2900$, flow remain closer to the wall than their counterparts in the $Re_\theta = 1430$ flow. This is in agreement with the profiles of $\lambda_2'(z)$ and $\omega_1'(z)$ shown in figure 4. Thus, increasing Re_θ 'squeezes' the vortical structures toward the wall whereas microbubbles 'push them away' from the wall. The net result of these two opposing effects determines the amount of skin friction reduction by the microbubbles. The displacement action by the microbubbles is a result of the local positive velocity divergence, $\nabla \cdot \boldsymbol{U}$, created by their concentration gradients as was discussed by FE. The instantaneous local $\partial_i U_i$ was computed at the pressure grid points using the staggered velocity components U_i via a second-order central finite-difference scheme. Spatial averaging in the spanwise (y) direction and time averaging of $\partial_i U_i$ were performed to produce the profile of $\langle \partial_i U_i \rangle(z)$ at $x = 18.9$ shown in figure 7(*a*). Figure 7 shows that:

(*a*) the microbubbles create a larger $\nabla \cdot \boldsymbol{U}$ in the lower-Reynolds-number ($Re_\theta = 1430$) SDTBL than that for $Re_\theta = 2900$, and the peak of $\nabla \cdot \boldsymbol{U}$ for the former is shifted slightly away from the wall relative to that of the latter;

(*b*) $\nabla \cdot \boldsymbol{U}$ is positive for both flows because $\langle \partial_z U_3 \rangle > 0$ and $\langle \partial_x U_1 \rangle < 0$ and the magnitude of the former is larger than that of the latter.

Figure 8(*a*) shows the profiles of bubble mean concentration $\langle C \rangle$ at three different streamwise stations $x = 5$, 14 and 18.9. Note that the profile at $x = 5$ is from case C of FE since for cases B and D of the current manuscript we had only stored mean profiles at $x = 14$ and 18.9. The profiles of $\langle C \rangle$ at $x = 14$ and 18.9 show a peak at about $z = 1$, which corresponds to $z^+ = 356$ for $Re_\theta = 1430$, and $z^+ = 785$ for $Re_\theta = 2900$. This means that, in both cases C and D, the peak of $\langle C \rangle$ occurs outside the near-wall region ($0 < z^+ < 100$). The position of this peak is a result of the reinjection of bubbles inside the computational domain. Bubbles exiting the computational domain are reinjected according to a semi-Gaussian law in the streamwise direction, which is nearly zero for $x > 10$, and uniformly distributed in the spanwise y-direction and in the wall-normal z-direction for $0 < z < \delta_0 = 1$. The volume fraction of bubbles

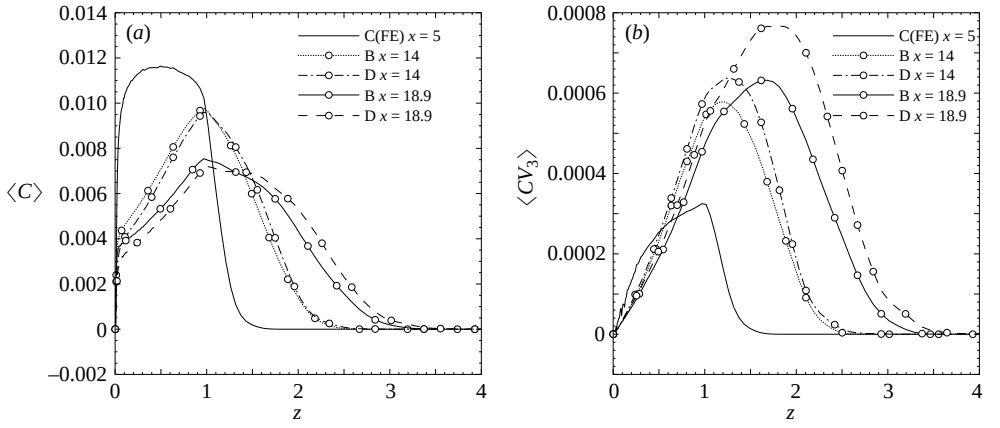

FIGURE 8. Profiles of mean bubble concentration $\langle C \rangle$ and bubble-phase wall-normal average velocity $\langle CV_3 \rangle$ at $x = 5,\ 14$ and 18.9 for $Re_\theta = 1430$ and $Re_\theta = 2900$.

exiting the computational domain per time step is only 0.009 % of the average void fraction, ϕ_v. The bubbles disperse in the z-direction as they move downstream, as shown in Figures 8(a) and 8(b), depicting the profiles of $\langle C \rangle$ and the bubble flux in the wall-normal direction $\langle CV_3 \rangle$.

In order to explain how the gradients of bubble concentration, created by the bubbles' interactions with the vortical structures, generate positive $\boldsymbol{\nabla \cdot U}$ we examine the continuity equation (2.1) by rewriting it as

$$\frac{\partial U_i}{\partial x_i} = \frac{[\mathrm{D}C/\mathrm{D}t]}{(1-C)} = \frac{1}{(1-C)}\left[\partial C/\partial t + U\partial C/\partial x + V\partial C/\partial y + W\partial C/\partial z\right]. \tag{3.2}$$

We now examine the instantaneous behaviour of the four terms in the square brackets on the right-hand side of (3.2). Figure 9(a) shows the instantaneous z profiles of $W\partial C/\partial z$ and $\boldsymbol{\nabla \cdot U}$ locally averaged in the y-direction, at $x = 18.9$ and $t = 40$ for $Re_\theta = 1430$. This region is within the sweep zone depicted in figure 10 and will be discussed below. Figures 9(b) and 9(c) show the corresponding profiles of $U\partial C/\partial x$ and $V\partial C/\partial y$. It is seen that the amplitudes of the fluctuations of $W\partial C/\partial z$ and $\boldsymbol{\nabla \cdot U}$ are of the same order of magnitude whereas those of $U\partial C/\partial x$ and $V\partial C/\partial y$ are an order of magnitude smaller. The fluctuations of $\partial C/\partial t$ (not shown) display as many positive as negative peaks, as expected, with amplitudes of the same order of magnitude as those of $W\partial C/\partial z$. It should be also noted that in the region close to the wall ($z \leqslant 0.2$ or $z^+ \leqslant 71$) the positive peaks of $W\partial C/\partial z$ occur at the same z locations of most (75 %) of the large (> 0.05) peaks of $\boldsymbol{\nabla \cdot U}$.

In order to explain the mechanisms responsible for these characteristics of $W\partial C/\partial z$, we show in figure 10(a) the instantaneous (at $t = 40$) contours of the streamwise vorticity, ω_1, together with the bubble locations and velocity vectors, for $Re_\theta = 1430$, in a vertical (y, z)-plane at $x = 18.9$, in a small zone ($0.45 \geqslant z \geqslant 0$ and $4.6 \geqslant y \geqslant 4.1$) close to the wall. Figure 10(b) shows the instantaneous contours of the fluid U_3 or W velocity together with the bubble locations and velocity vectors at the same time and zone of figure 10(a). We selected this zone because it contains a typical near-wall quasi-streamwise vortical structure. Focusing in figure 10(a) on the counter-clockwise vortex centred at $y = 4.28$ and $z = 0.15$ we see that bubbles are being advected in the down-draught (or sweep) side toward the wall, and carried away from the wall in the up-draught (or ejection) side of the vortex. The contours of the fluid W velocity

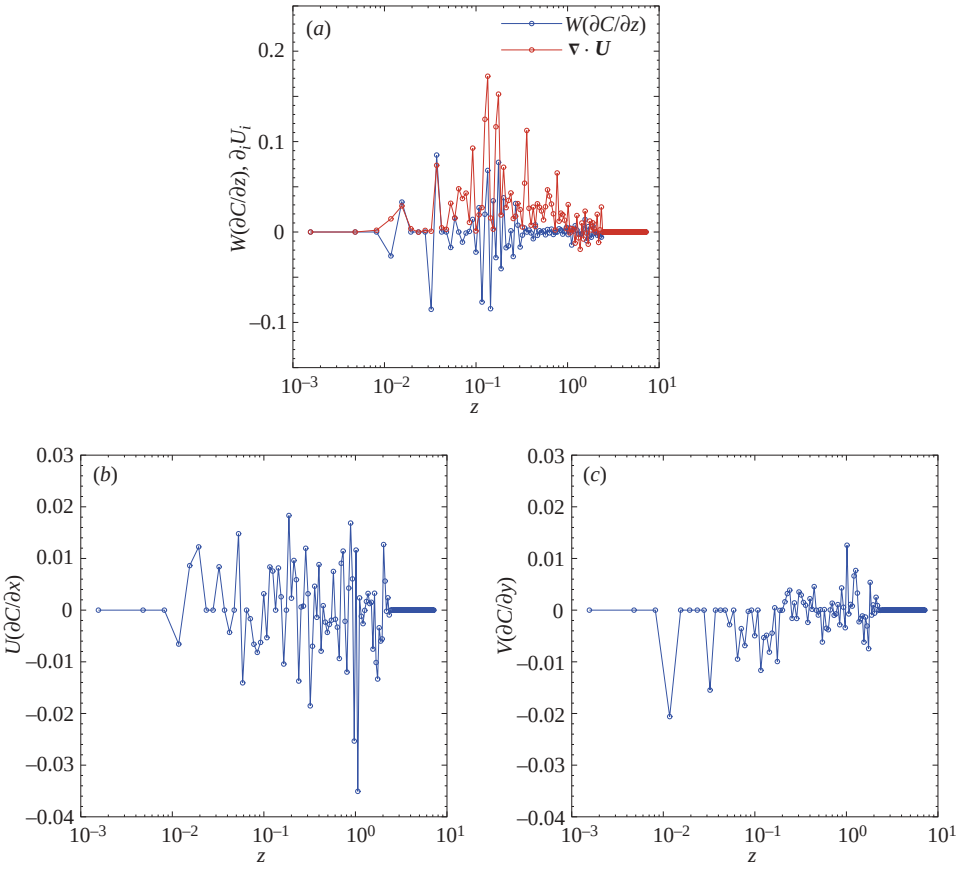

FIGURE 9. Instantaneous profiles of $\nabla \cdot \boldsymbol{U}$, $W\,\partial_z C$, $U\,\partial_x C$ and $V\,\partial_y C$ locally averaged along horizontal z lines in the spanwise y-direction, at $x = 18.9$, in the sweep zone between $y = 4.16$ and 4.22 at $t = 40$ for $Re_\theta = 1430$.

in figure 10(b) clearly display the sweep and ejection regions straddling the vortex and how the sweep ($W < 0$) increases the bubble concentration closer to the wall ($\partial C/\partial z < 0$), and the ejection ($W > 0$) increases the bubble concentration away from the wall ($\partial C/\partial z > 0$). The schematic in figure 10(c) depicts this physical mechanism which is responsible for the above described behaviour of $W\partial C/\partial z$ (figure 9(a)), and thus resulting in a positive $\langle \partial W/\partial z \rangle$ as shown in figure 7. We have also plotted (not shown here) the contours of the vorticity, ω_1, and W velocity as in figure 10(a) but for $Re_\theta = 2900$. We find that the sizes of the vortical structures are reduced, as expected, with the increase of Re_θ and the corresponding increase of the strain rate $\partial U_1/\partial z$. The structures are also squeezed toward the wall in the zone $z < 0.1$ as discussed earlier. The magnitudes of the bubble velocity vectors in the selected vertical plane are considerably reduced relative to those in figure 10 due to the increased bubble velocity in the streamwise direction owing to the advection by the carrier fluid. The result is the increase of the magnitude of the negative $\partial U_1/\partial x$ for $Re_\theta = 2900$ in figure 7.

In summary, our DNS results show that increasing the Reynolds number decreases the percentage of drag reduction. Increasing Re_θ 'squeezes' the quasi-streamwise

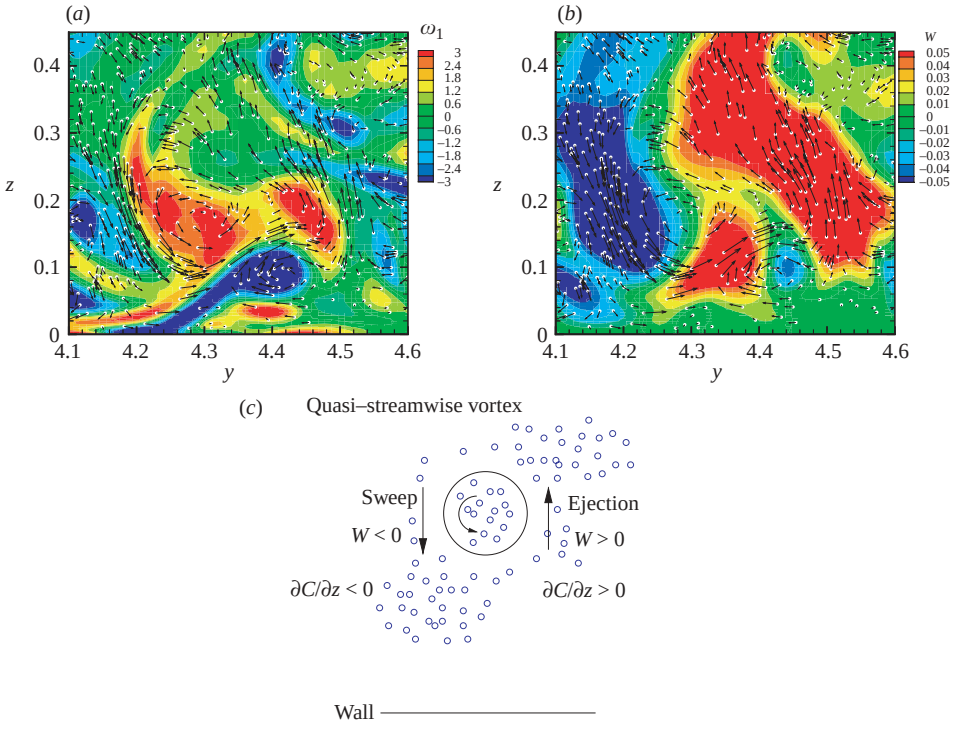

FIGURE 10. (*a*) Instantaneous contours at $t = 40$ of streamwise vorticity, ω_1, and vectors of bubble velocity for $Re_\theta = 1430$ near a quasi-streamwise vortex at $x = 18.9$. (*b*) Instantaneous contours of wall-normal fluid velocity, W, and vectors of bubble velocity in the same zone as in (*a*). (*c*) Schematic of bubble accumulation near a vortex.

vortical structures toward the wall whereas the microbubbles 'push them away' from the wall. The net result of these two opposing effects determines the amount of skin friction reduction by the microbubbles. The displacement action by the microbubbles is a result of the local positive velocity divergence, $\nabla \cdot \boldsymbol{U}$, created by their concentration gradients. Thus, the volume fraction of bubbles that is responsible for the reduction of skin friction in a SDTBL at a given Reynolds number is not sufficient to produce the same amount of reduction in skin friction at higher Reynolds number.

This work was supported by ONR Grant No. N00014-05-1-0059, and the computations were performed on IBM-Power4+ located at the Naval Oceanographic Office at NASA's John C. Stennis Space Center (NAVO-MSRC, Mississippi), and on CRAY-T3E located at U.S. Army High Performing Computing Research Center (AHPCRC, Minnesota).

Appendix. Numerical method for the coupled bubble–fluid phases

In order to write the Poisson equation for pressure in terms of pressure fluctuations, p, it is necessary to remove the hydrostatic pressure from the total pressure P in the momentum equation of the carrier fluid (2.2) as follows (Druzhinin & Elghobashi

1998):

$$p = P + g\int_0^{x_3}(1-\overline{C})\,\mathrm{d}x_3 \tag{A 1}$$

where the gravitational acceleration is assumed in the negative x_3-direction ($g_i = -g\delta_{iz}$), and $\overline{C}(x_3, t)$ represents the instantaneous ensemble-average of C in the horizontal (x, y)-plane at distance x_3 from the wall. The sum of the pressure gradient and gravity terms in the fluid momentum equation in the x_3-direction, using (A 1), thus becomes

$$\begin{aligned}-(1-C)\partial_{x_3}P-(1-C)g &= -(1-C)\partial_{x_3}p+(1-C)\partial_{x_3}\left[g\int_0^{x_3}(1-\overline{C})\,\mathrm{d}x_3\right]-(1-C)g\\ &= -(1-C)\partial_{x_3}p\ -\overline{C}(1-C)g.\end{aligned} \tag{A 2}$$

Substituting (A 2) in (2.2), the fluid momentum equations can be written as

$$\begin{aligned}\partial_t[(1-C)U_i]+\partial_j[(1-C)U_iU_j] = &-\partial_i[(1-C)p]\ +\nu\,\partial_j[(1-C)(\partial_jU_i+\partial_iU_j)]\\ &-f_i+p\partial_i(1-C)\ +\overline{C}(1-C)g_i.\end{aligned} \tag{A 3}$$

The bubble–fluid coupling force f_i in (A 3) is computed as the net force per unit mass of fluid imparted on the fluid by $N_b(\boldsymbol{x}, t)$ bubbles within the computational control volume $V_c(\boldsymbol{x})$ as

$$-f_i = C\left(\frac{\mathrm{D}U_{s,i}}{\mathrm{D}t}-g_i\right) = \sum_{b=1}^{N_b(\boldsymbol{x},t)}\left[\frac{[\pi d_b^3/6]}{\mathscr{V}_c(\boldsymbol{x})}\left(\frac{\mathrm{D}U_{s,i}(\boldsymbol{x}_b(t))}{\mathrm{D}t}-g_i\right)\right], \tag{A 4}$$

where d_b is the bubble diameter. Furthermore, because the bubble location $\boldsymbol{x}_b(t)$ does not coincide in general with the position $\boldsymbol{x}$ of any grid nodes, the term under summation in (A 4) was linearly projected to the eight grid nodes surrounding the bubble b prior to the summation.

The solution algorithm starts by defining RU_i as

$$\begin{aligned}RU_i \equiv &-\partial_j[(1-C)U_iU_j]+\nu\,\partial_j[(1-C)(\partial_jU_i+\partial_iU_j)]\\ &-f_i+p\,\partial_i(1-C)\ +\overline{C}(1-C)g_i\end{aligned} \tag{A 5}$$

and $\breve{U}_i$ and $\breve{p}$ as

$$\breve{U}_i \equiv (1-C)U_i \quad \text{and} \quad \breve{p} \equiv (1-C)p. \tag{A 6}$$

Thus, (A 3) can be rewritten as,

$$\partial_t\breve{U}_i = -\partial_i\breve{p}\ + RU_i. \tag{A 7}$$

The RU_i terms were discretized in space in an Eulerian framework on a staggered mesh using a second-order central-difference scheme, except for the mean advection terms, which were evaluated via a fifth-order upwind differencing scheme. Time integration of (A 7), without the pressure gradient term, was performed using the Adams–Bashforth scheme,

$$\frac{\breve{U}_i^* - \breve{U}_i^n}{\Delta t} = \frac{3}{2}RU_i^n - \frac{1}{2}RU_i^{n-1}, \tag{A 8}$$

where $\breve{U}_i^*$ is an approximate value of $\breve{U}_i^{n+1}$ before applying the pressure correction (A 17) below, and the superscipts indicate the time level, i.e. $\breve{U}_i^n = \breve{U}_i(\boldsymbol{x}, t^n)$. The time

step used was $\Delta t^+ = 0.075$ in cases A and B, and $\Delta t^+ = 0.15$ in cases C and D. The following Poisson equation for pressure:

$$\partial_{ii}^2 \breve{p}^{n+1} = \frac{1}{\Delta t}\left[\partial_i \breve{U}_i^* - \partial_i \breve{U}_i^{n+1}\right], \tag{A 9}$$

written in finite-difference form (Gerz, Schumann & Elghobashi 1989) was solved using a cosine transform in the streamwise direction (Wilhelmson & Ericksen 1977), a fast Fourier transform (FFT) in the spanwise direction, and Gauss elimination in the wall-normal direction (Schmidt, Schumann & Volkert 1984). The discrete cosine and Fourier transforms were computed using the FFTW library by Frigo & Johnson (2005).

In order to compute the right-hand side of (A 9), $\partial_i \breve{U}_i^{n+1}$ was evaluated using the fluid continuity equation (2.1), as

$$\partial_i \breve{U}_i^{n+1} = \partial_t C^{n+1}, \tag{A 10}$$

where $\partial_t C^{n+1}$ was evaluated as

$$\partial_t C^{n+1} = \frac{C^{n+1} - C^n}{\Delta t}. \tag{A 11}$$

In (A 11), the local concentration C^n was computed from the instantaneous local number of bubbles $N_b(\boldsymbol{x}, t^n)$ in a given computational cell as

$$C(\boldsymbol{x}, t^n) = N_b(\boldsymbol{x}, t^n)\frac{[\pi d_b^3/6]}{\mathscr{V}_c(\boldsymbol{x})}, \tag{A 12}$$

whereas C^{n+1} was obtained by solving the bubble-phase continuity equation (Drew 1983; Zhang & Prosperetti 1997),

$$\partial_t C + \partial_j C\overline{V}_j = 0, \tag{A 13}$$

using the Adams–Bashforth scheme:

$$\frac{C^{n+1} - C^n}{\Delta t} = \frac{3}{2}RC^n - \frac{1}{2}RC^{n-1}, \tag{A 14}$$

where RC is defined as,

$$RC \equiv -\partial_j C\overline{V}_j. \tag{A 15}$$

The bubble-phase instantaneous local velocity $\overline{V}_i$ in (A 13) was evaluated by ensemble averaging the bubbles velocities within the local computational cell:

$$\overline{V}_i(\boldsymbol{x}, t) = \frac{1}{N_b(\boldsymbol{x}, t)}\sum_{b=1}^{N_b(\boldsymbol{x},t)} V_i(\boldsymbol{x}_b(t)). \tag{A 16}$$

Finally, U_i^{n+1} was updated by accounting for the pressure correction as

$$U_i^{n+1} = [\breve{U}_i^* - \Delta t\, \partial_i\, \breve{p}^{n+1}] \,/\, [(1 - C)^{n+1}]. \tag{A 17}$$

At each grid point of the computational mesh and at each time step we checked that the continuity equation of the fluid (2.1), is satisfied. The maximum and minimum values of the left-hand side of (2.1) computed instantaneously at each grid point of the computational mesh are of the order of 10^{-13}.

The bubble equation of motion (2.3) was solved in time for each computational bubble using the Adams–Bashforth scheme to compute the bubble velocity. The fluid velocity, $\boldsymbol{U}_s$, fluid vorticity, $\boldsymbol{\Omega}_s$, and fluid Lagrangian derivative, $\mathrm{D}\boldsymbol{U}_s/\mathrm{D}t$, at the bubble location, needed to solve (2.3), were computed via a fourth-order-accurate fully three-dimensional Hermite cubic interpolation polynomial adapted to a non-uniform mesh

(see Ferrante 2004, Appendix D). The fluid Lagrangian derivatives, $\mathrm{D}U_i/\mathrm{D}t$, at the staggered grid points, needed for the interpolation of $\mathrm{D}\boldsymbol{U}_s/\mathrm{D}t$, were computed using (A 3) and (2.1) as

$$\frac{\mathrm{D}U_i}{\mathrm{D}t} = \frac{1}{1-C}\{-\partial_i[(1-C)p] + \nu\,\partial_j[(1-C)(\partial_j U_i + \partial_i U_j)] - f_i + p\,\partial_i(1-C) + \overline{C}(1-C)g_i\}. \quad (A\,18)$$

The bubbles positions were then updated from the time integration of the bubble velocity ($\mathrm{d}\boldsymbol{x}_b/\mathrm{d}t = \boldsymbol{V}$) as

$$\boldsymbol{x}_b^{n+1} = \boldsymbol{x}_b^n + \frac{\Delta t}{2}[\boldsymbol{V}^{n+1} + \boldsymbol{V}^n]. \quad (A\,19)$$

REFERENCES

DeGraaff, D. & Eaton, J. 2000 Reynolds-number scaling of the flat-plate turbulent boundary layer. *J. Fluid Mech.* **422**, 319–346.

Drew, D. A. 1983 Mathematical modeling of two-phase flow. *Annu. Rev. Fluid Mech.* **15**, 261–291.

Druzhinin, O. & Elghobashi, S. 1998 Direct numerical simulations of bubble-laden turbulent flows using the two-fluid formulation. *Phys. Fluids* **10**, 685–697.

Ferrante, A. 2004 Reduction of skin friction in a microbubble-laden spatially-developing turbulent boundary layer over a flat plate. PhD Thesis, University of California, Irvine.

Ferrante, A. & Elghobashi, S. 2004*a* Effects of bubble diameter on drag reduction in a microbubble-laden spatially-developing turbulent boundary layer over a flat plate. *Bull. Am. Phys. Soc.* **49**, 116.

Ferrante, A. & Elghobashi, S. 2004*b* On the physical mechanisms of drag reduction in a spatially-developing turbulent boundary layer laden with microbubbles. *J. Fluid Mech.* **503**, 345–355 (referred to herein as FE).

Ferrante, A. & Elghobashi, S. 2004*c* A robust method for generating inflow conditions for direct simulations of spatially-developing turbulent boundary layers. *J. Comput. Phys.* **198**, 372–387.

Frigo, M. & Johnson, S. G. 2005 The Design and Implementation of FFTW3. *Proc. IEEE* **93**, 216–231.

Gerz, T., Schumann, U. & Elghobashi, S. 1989 Direct numerical simulation of stratified homogeneous turbulent shear flows. *J. Fluid Mech.* **200**, 563–594.

Hinze, J. 1955 Fundamentals of the hydrodynamic mechanism of splitting in dispersion processes. *AIChE J.* **1**, 289–295.

Jeong, J. & Hussain, F. 1995 On the identification of a vortex. *J. Fluid Mech.* **285**, 69–94.

Jeong, J., Hussain, F., Schoppa, W. & Kim, J. 1997 Coherent structures near the wall in a turbulent channel flow. *J. Fluid Mech.* **332**, 185–214.

Madavan, N., Deutsch, S. & Merkle, C. 1985 Measurements of local skin friction in a microbubble-modified turbulent boundary-layer. *J. Fluid Mech.* **27**, 237–256.

Martinez-Bazan, C., Montanes, J. & Lasheras, J. 1999 On the breakup of an air bubble injected into a fully developed turbulent flow. Part 1. Breakup frequency. *J. Fluid Mech.* **401**, 157–182.

Pal, S., Merkle, C. & Deutsch, S. 1988 Bubble characteristics and trajectories in a microbubble boundary layer. *Phys. Fluids* **31**, 744–751.

Prosperetti, A. & Zhang, D. 1995 Finite-particle-size effects in disperse two-phase flows. *Theor. Comput. Fluid Dyn.* **7**, 429–440.

Schmidt, H., Schumann, U. & Volkert, H. 1984 Three dimensional, direct and vectorized elliptic solvers for various boundary conditions. *Rep.* 84-15. DFVLR-Mitt.

Silberman, E. 1957 Production of bubbles by the disintegration of gas jets in liquid. *Fifth Midwestern Conference on Fluid Mechanics*, vol. 1, pp. 263–284. University of Michigan, St. Anthony Falls Hydraulic Laboratory, Tech. Paper 12, Series A.

Wilhelmson, R. B. & Ericksen, J. H. 1977 Direct solutions for Poisson's equation in three dimensions. *J. Comput. Physics* **25**, 319–331.

Zhang, D. Z. & Prosperetti, A. 1997 Momentum and energy equations for disperse two-phase flows and their closure for dilute suspensions. *Intl J. Multiphase Flow* **23**, 425–453.